Structure and NOx Emissions of Stratified Hydrogen-Air Flames Stabilized on a Coaxial Injector

Maxime Leroy, Clément Mirat, Antoine Renaud, Stefano Puggelli, Stephan Zurbach, Ronan Vicquelin

Structure and NOx emissions of stratified hydrogen-air flames stabilized on a coaxial injector

Maxime Leroy*
Université Paris-Saclay,
CNRS, CentraleSupélec, Laboratoire EM2C,
91190, Gif-sur-Yvette, France.
Safran Tech
rue des Jeunes Bois, Châteaufort,
78114, Magny-les-Hameaux, France
Email: maxime.leroy@centralesupelec.fr

Clément Mirat
Université Paris-Saclay,
CNRS, CentraleSupélec, Laboratoire EM2C,
91190, Gif-sur-Yvette, France.
Email: clement.mirat@centralesupelec.fr

Antoine Renaud
Université Paris-Saclay,
CNRS, CentraleSupélec, Laboratoire EM2C,
91190, Gif-sur-Yvette, France.
Email: antoine.renaud@centralesupelec.fr

Stefano Puggelli
Safran Tech
rue des Jeunes Bois, Châteaufort,
78114, Magny-les-Hameaux, France
Email: stefano.puggelli@safrangroup.com

Stephan Zurbach
Safran Tech
rue des Jeunes Bois, Châteaufort,
78114, Magny-les-Hameaux, France
Email: stephan.zurbach@safrangroup.com

Ronan Vicquelin
Université Paris-Saclay,
CNRS, CentraleSupélec, Laboratoire EM2C,
91190, Gif-sur-Yvette, France.
Email: ronan.vicquelin@centralesupelec.fr

ABSTRACT

In recent years, the need for low-carbon power has seen hydrogen emerge as a potential fuel to replace conventional hydrocarbons in combustion to limit CO_2 emissions in several sectors, including aeronautics. The challenges posed by hydrogen combustion are similar to the issues of kerosene flames but more challenging, like nitrogen oxide (NO_x) emissions and flame flashback. One potential solution to address these problems is to burn a rich mixture of hydrogen and air in globally lean conditions on a coaxial injector to

*Address all correspondence to this author

obtain a stable and staged combustion and attempt to reduce emissions. In this article, the evolution of NO_x production as more air is mixed into the fuel is studied, as well as the changes in flame size and structure. In particular, the appearance of a secondary flame front is observed and increasing the proportion of air in the fuel mixture both shortens the flame and reduces the NO_x emission index. Additionally, the effect of the global equivalence ratio and flame thermal power are studied. Finally, existing models for NO_x emission of hydrogen flames on a coaxial injector based on average flame residence time and strain rate are tested and shown to have promising results.

NOMENCLATURE

$_1$ Subscript for central (fuel) channel

$_2$ Subscript for annular (air) channel

A Channel cross-sectional area (m^2)

d Channel diameter ()mm)

e Inner channel lip thickness (mm)

J Momentum flux ratio

L_f Length of the diffusion flame front [m]

L_p Length of the premixed flame front [m]

$\dot{m}$ Channel mass flow rate ($kg{\cdot}s^{-1}$)

$\mathcal{P}_{th}$ Flame thermal power (kW)

Re Reynolds number $Re = \frac{dU}{\nu}$

ρ Density ($kg{\cdot}m^{-3}$)

Φ Equivalence ratio

u Channel bulk velocity ($m{\cdot}s^{-1}$)

NO_x Nitrogen oxides NO and NO_2

$EINO_x$ NO_x emission index (g/kgH_2)

OH* Excited OH radical

INTRODUCTION

The drive to reduce CO_2 emissions of the aeronautical sector has seen hydrogen get increasing attraction for its potential of carbon-free combustion. However, the high combustion temperatures of hydrogen, as well as its high laminar flame speed, generate a few challenges to be tackled, such as nitrogen oxides (NO_x) emission and stability. These challenges are not new, as burners using classical fuels such as natural gas or kerosene have required NO_x reductions, while keeping stable flames. As a result, many concepts have been developed in the past, such as Lean Premixed [1], Lean Direct injection (LDI)[2] or Rich-Burn Quick-Mix Lean-Burn (RQL) [3]. These concepts can then be adapted for use in hydrogen combustion, and adaptations of LDI [4] and Lean Premixed [5, 6] have been studied, alongside new concepts such as micromix [7, 8].
Here, we will study a derivative of the RQL concept, which consists from a theoretical point of view of injecting first fuel and air to burn a rich mixture (in a technically premixed regime), then using a quick addition of air to finish combustion, and reach a globally lean mixture. The advantages of this technique for hydrogen are highlighted by the flame properties computed with the CRECK mechanism [9, 10] for standard pressure and temperature and shown in Fig. 1. RQL avoids the range of equivalence ratios around stoichiometry where NO_x production is maximal because of the Zel'dovich or thermal reaction pathway. Additionally, the prompt NO pathway from CH radical in hydrocarbons flames, which produces an increasing amount of NO_x with equivalence ratio, is not active in H_2 combustion [11]. It is also apparent that the maximum laminar burning velocity is located around the equivalence ratio of 2, making such rich premixed flames hard to blow off.

Hydrogen burners using a conventional RQL design have been studied by Göke et al.[12]. Taking advantage of the H_2 flame properties such as ease of ignition and strain rate resistance, a more compact combustor can be considered along with a different injector configuration such as a coaxial injector. Several works [13, 14] have recently shown various flame types stabilized on coaxial injectors with pure hydrogen injected in the central channel. The present work investigates using a coaxial burner as a RQL concept where a staged air injection with a rich premixed mixture and a coaxial stream is considered. Minakawa & Yuasa [15] studied a similar injector that showed

potential for low-NO_x flames.

The observed flames stabilized on the coaxial injector share several features with non-premixed diffusion jet flames extensively studied in the literature. The seminal work of Peters and Donnerhack [16] provides analysis for NO_x production from the Zel'dovich mechanism in unconfined jet diffusion flames, accounting for a flame residence time, which highlights the relationship between the flame length, the jet velocity, and NO_x production. Their analytical model found the $EINO_x$ to scale as ${L_f}^3/({u_1}{d_1}^2)$, which can be interpreted as a residence time. Subsequent works have extended it to more complex cases, such as diluted or coaxial flames, while considering the effect of strain or improving the residence time modeling. Chen and Driscoll [17] have combined the analytical model from Peters and Donnerhack [16] with the flame length model from Dahm and Mayman [18] to explain how the addition of coaxial air achieved reductions of NO_x emissions by shortening the flame. Taking into account the effect of the Damköhler number allowed to show that the normalized emissions $EINO_x/({L_f}^3/({u_1}{d_1}^2))$ scaled as the $(u_1/d_1)^n$ with n = 1/2. Driscoll et al. [19] then investigated flame dilution with helium and compared the separate effect of coaxial air with that of rich premixing. This was further extended when Chen and Kollman [20] studied hydrogen flames with coaxial air, for moderate u_1/u_2 ratios. They highlighted that in that case the flame volume V_f should be directly used instead of ${L_f}^3$ to more accurately describe the flame zone. With this approach and replacing u_1/d_1 with $(u_1 - u_2)/d_1$ to take into account the effect of coaxial flow, they were again able to collapse their result on a single slope in a numerical study that appeared to follow another 1/2 power law. In addition, Weiland et al. [21] studied and modeled the effect of N_2 dilution on hydrogen coaxial flames, showing that combining coaxial air and dilution reduces flame length and emissions.

These studies provide an extensive basis for studying RQL-like jet flames stabilized on a coaxial injector. However, except for [15], no works could be found about the study of flame length and NO_x emissions in staged hydrogen coaxial flames to tie them with existing knowledge on hydrogen flames. Furthermore, the evolution of the flame structure as the proportion of air in the central channel increases has yet to be studied. As a result, this work on rich-premixed hydrogen-air

coaxial flames focuses on the effect of air staging on the flame length and NO_x emission. The flame length is of prime importance in designing a compact aero-engine, but will also be shown to be an essential factor in NO_x production as in other jet flames studied in the literature.

The work is presented in the following sections. The second section presents the experimental setup used to produce and study hydrogen flames at a laboratory scale at ambient pressure and the post-processing method used for flame measurement. In Sec. 3, we first present the topology of the flames we obtain and describe the appearance of a secondary flame front due to the staged injection of air. Then, we study the evolution of flame lengths in unconfined jets under various degrees of staging. In the fourth section, the effect of staging on NO_x is investigated, and the observed evolution is compared to existing models. Finally, in Sec. 5, we study the effect of thermal power and global equivalence ratio variations and attempt to find a common model that can account for the change of all these parameters.

1 EXPERIMENTAL SETUP

This section presents the studied configuration (combustion chamber and injector), the controlling parameters, and the employed diagnostics.

1.1 Combustion chamber

The combustion chamber used in this study is the same as the one used in [14], and [22, 23], with the exception that the exit section is reduced to a 30 x 30 mm square in order to avoid recirculation of exterior air induced by the entrainment of the flame jet, as described in Fig. 2 (a). The gas analyzer used is the same as the one in [14], and the injector is a coaxial injector of external diameter $d_2 = 20$ mm and two variants of internal diameter with either $d_1 = 6$ mm or $d_1 = 10$ mm. Using the $d_1 = 6$ mm diameter allows to establish a fully developed flow while using the $d_1 = 10$ mm does not, due to the change in section occuring near the end of the injector tube. In the annular channel, a centering piece located 76 mm upstream of the exit plane causes a developing flow profile.

1.2 Injector

The injection is controlled by three parameters: the flame thermal power $\mathcal{P}_{th}$ which, sets the mass flow rate of hydrogen in the central channel $\dot{m}_{1,H_2}$, the rich central equivalence ratio Φ_1, that determines the premixed mass flow rate of air in the central channel $\dot{m}_{1,air}$ and the global equivalence ratio Φ_{tot}, that sets the mass flow rate in the annular channel $\dot{m}_2$:

$$\Phi_1 = s\frac{\dot{m}_{1,H_2}}{Y_{2,O_2}\dot{m}_{1,air}}, \Phi_{tot} = s\frac{\dot{m}_{1,H_2}}{Y_{2,O_2}(\dot{m}_{1,air}+\dot{m}_2)} \tag{1}$$

with s = 8, the mass stoichiometric ratio and Y_{2,O_2} = 0.233 the oxygen mass fraction in the oxidizer stream

Once these flow rates are set, we can compute the momentum flux ratio J:

$$J = \frac{\rho_2 {U_2}^2}{\rho_1 {U_1}^2} = \frac{A_1^2\rho_1}{A_2^2\rho_2}\frac{\dot{m}_2^2}{\dot{m}_1^2} \tag{2}$$

An overview of the range of values for these parameters and others for is provided in Table 1.

1.3 Diagnostics

The flame structure is observed using OH* chemiluminescence. A Princeton Instruments PI-MAX4 intensified CCD camera is equipped with a NIKKOR 105 mm UV objective and an Asahi SPECTRA XBPA310 310 $\pm$ 5 nm bandpass filter. The aperture is fixed at f/8.0, and the exposure time is $\Delta t = 15$ ms. Fifty images are averaged together to construct the mean images. Afterwards, the images are post-processed by inverse Abel transform to visualize the flame front, and a Gaussian filter of σ = 0.9 pixels is applied to lessen the noise induced by this transform.

Exhaust gas composition analysis is performed using a HORIBA VA-5111 multi-component gas analyzer unit associated with a VS-5000 series sampling unit. The measured molar fraction of the species of interest are O_2, using a paramagnetic sensor, and NO, using an NDIR sensor. Before being analyzed, the exhaust gases are dried through a condenser. Measurement of total

NO_x (NO+ NO_2) is obtained using a NO_2 to NO converter upstream of the analyzer unit that a switch can toggle. The NO sensor has a range of 0-500 ppm and a manufacturer-specified repeatability of $\pm$ 2.5 ppm. The sensors are calibrated using calibration gas bottles with a 3% precision on composition.

In order to account for potential variations in the exit plane, three measurements of gas composition are taken, one at the center of the exit section, one at r = 6 mm, and one at r = 12 mm. The results are averaged to obtain the final value. The NO_x emission index (EINOx) in g/kgH_2 is used to produce a metric under which all flames can be compared:

$$EINO_x = X_{NO_x,wet} \frac{M_{NO_2}}{\bar{M}(\Phi_{tot})} \frac{\dot{m}_{tot}}{\dot{m}_{H_2}} \tag{3}$$

As in [19], the molar mass of NO_2 is used to calculate $EINO_x$ as most NO is converted to NO_2 in the atmosphere. The average molar mass of the flue gas $\bar{M}$ is obtained on the basis of a one-step reaction at the injected equivalence ratio. Furthermore, $X_{NO_x,wet}$ is obtained from the dry NO_x measurement using the expected water exhaust mole fraction from a one-step reaction at the given equivalence ratio, as it could not be measured.

$$X_{NO_x,wet} = X_{NO_x,dry}(1 - X_{H2O}(\Phi_{tot})) \tag{4}$$

Gas molar fractions are measured once the chamber reaches thermal equilibrium, indicated by the stabilization of the wall temperature, to avoid possible transient effects. In addition, the mole fraction of unburned hydrogen is measured using a Madur SENMA electrochemical H_2 sensor with a 0-2000 ppm range. No significant levels ($<$30 ppm) of unburned hydrogen are detected in the flames in this study, indicating complete combustion.

1.4 Flame length measurement

Previous studies [18, 17, 19] have shown that flame length is of particular interest when studying NO_x in jet flames. We, therefore, estimate these flame lengths. We choose to use OH* chemiluminescence imagery as the hot water vapor produced by H_2 combustion radiates in the near-infrared region [24] and emits visible light above the effective reaction region of the flame. Our approach is similar to the one used in [25], and thresholding with Otsu's method [26] is employed.

Two different cases must be separated. In the first case, the flame displays one flame front, and the Otsu method is used on the OH* image to separate the dark pixels in the background from the flame. This technique isolates the brighter pixels of the OH* chemiluminescence image and allows us to capture the contour of the flame. The height of the highest pixel of this contour provides an estimate of the flame length. In the second case, two flame fronts are apparent and there is a need to separate the premixed inner flame front from the outer flame front. A multiple-threshold variant of the Otsu method is used to detect the two flames based on their brightness. Two thresholds are used, allowing us to obtain two different classes of pixels within the flames that capture the outer and inner flame front, respectively. The two flame front lengths are measured based on these thresholds. The effect of this thresholding method is illustrated in Figs. 3 and 4. Figure 3 shows the histogram of a flame with two flame fronts and the thresholds obtained by multiple Otsu thresholding. It shows three distinct categories of pixels: a sharp peak near zero corresponding to the background, a weaker peak of median intensity with a normalized intensity of around 0.4, and a smaller group of very high-intensity pixels centered around a normalized intensity of 0.7. The two thresholds obtained by the Otsu method are also traced in the histogram and separate the three different groups of pixels. Observation of the associated OH* image in Fig. 4 allows us to verify that these groups of pixels correspond to the flame's discernible features. The contour drawn from the first threshold captures the longer diffusion flame, while the contour corresponding to the higher threshold captures the brighter pixels of the premixed flame front. As the brighter front can change as a function of the equivalence ratio, the attribution of each measure to each flame is based on its length: the shorter flame is the premixed one, and the longest is the diffusion flame.

Overall, these observations show that both flame fronts' lengths can be measured. As the Otsu thresholding is sensitive to the total number of pixels, the effect of cropping the background was studied and was found to diminish the flame length of the diffusion flame front by up to 5% after removing 90% of the width of the image where the flame was not present. In the rest of the study, the entire background is kept to maintain the same conditions for each image.

2 FLAME TOPOLOGY AND LENGTHS AT $\mathcal{P}_{th}$= 10 KW

2.1 RQL-like combustion stabilized above a coaxial injector

Using the coaxial injector described in Sec. 1, we obtain jet flames, of which an overview of the different visualizations is shown in Fig. 5. The particular example flame presents two flame fronts revealed by the inverse Abel transform. The shorter one is produced by the combustion of the rich premixed H_2/air mixture, while the longer one surrounds the first one and corresponds to a diffusion flame between burned gases from the first flame front and coflowing air. According to Fig. 1, the stoichiometric diffusion flame front is expected to be responsible for most of the NO_x emission.

The flames produced on this type of injector differ from the conventional and idealized RQL kind of flame as a hot diffusion flame front is still present after the cooler rich premixed flame. However, a quick transition from rich to lean burn should temper this high-NO_x route. Hence, as in any practical RQL system, a rapid mixing with the added air is primordial to reduce the time in contact with the stoichiometry line.

2.2 Appearance of the secondary flame front

As shown in Fig. 6, when the fuel changes from non-premixed hydrogen to a fuel-air blend, the premixed flame front does not appear immediately. The appearance of the premixed flame front is described more finely in Fig. 7, which shows the Abel-inverted OH* chemiluminescence images of flames between the central equivalence ratio Φ_1 = 3.5 where the first traces of the premixed flame front appear and Φ_1 = 2. The shortening of the diffusion flame front is discussed in the next section. The images in Figs. 6 and 7 show that the premixed flame front appears and gradually strengthens.

This is due to two factors. The first is that the flame needs to have a sufficient velocity to stabilize at the exit of the central channel. As shown in Fig. 1, the laminar burning velocity (and therefore the turbulent flame speed) increases as Φ_1 approaches 2, which makes it possible for flames to stabilize. The other factor is that with growing staging, the fraction of fuel being burned in the premixed flame increases as opposed to the diffusion front. Therefore, the production of OH* radical and the associated emission of light in the premixed flame front increases, making it more visible in OH* imaging. In addition, turbulence might cause partial extinction of the richer flames, decreasing the light in the premixed flame front. As a result, only when Φ_1 is below 2.5 is the flame front established at the same level of luminosity as the base of the diffusion flame front. Above this value, the flame front is fainter, and our detection algorithms struggle to separate it from the background, which is why no length measurement for the premixed front is reported in Fig. 7 for $\Phi_1 >$2.5.

Interestingly, the premixed flame front length in this series of flames remains somewhat constant. Assuming a conical Bunsen flame of base diameter d_1 and of height L_p, we can write the turbulent flame speed:

$$S_T = u_1 sin(\alpha) \rightarrow L_p \approx u_1 d_1/(2S_T) \tag{5}$$

where α is the flame half-angle. As Φ_1 increases, less air is conveyed in the central channel, and u_1 decreases, which would shorten the premixed flame. However, simultaneously, the turbulent flame speed proportional to the laminar burning velocity also decreases. Both trends compensate and explain the similar premixed flame heights in Fig. 7.

2.3 Flame length of unconfined coaxial jets

Flame lengths have been measured for various conditions of central equivalence ratio Φ_1 and global equivalence ratio Φ_{tot}. We report here the total flame length L_f corresponding to the diffusion flame front. The mass flow of hydrogen is fixed to yield a thermal power $\mathcal{P}_{th}$= 10 kW, and Φ_1 is varied between infinity (non-premixed injection) and 2, for Φ_{tot} between 0.3 and 0.9 by increasing

the flow rate of coaxial air. The coaxial jet flames are first observed in quiescent air with the combustion chamber removed to measure longer flames and without waiting for steady wall thermal conditions. With $\Phi_{tot} < 1$, the hydrogen combustion is complete with the injected air. To evaluate the potential influence of buoyancy, the dimensionless parameter ξ_L from Becker and Yamazaki [27] is calculated. Except for the longest non-premixed and Φ_1 = 6 flames, it is found to lie below 1.5, suggesting a negligible buoyancy effect.

Flame lengths normalized by internal diameter d_1 are plotted in Fig. 8 as a function of the momentum flux ratio $J^{-1/2}$, based on the observations of a linear relationship, in some conditions, between L_f/d and $J^{-1/2}$ by previous authors for various fuels and oxidizers [28, 25]. Isolines of global equivalence ratio Φ_{tot} are drawn between points of the same internal diameter d_1. Following these isolines, it appears that under the same global equivalence ratio, premixing fuel and air first increases the length of the flame between $\Phi_1 = \infty$ and Φ_1 = 6. Then, between Φ_1 = 6 and Φ_1 = 2, the flame length progressively becomes shorter. This evolution of flame length can be explained qualitatively by the evolution of both momentum flux ratio and stoichiometric mixture fraction Z_{st}, as described in [28]. As the staging is increased (reduction of Φ_1), the flow rate in the annular channel decreases while the flow rate in the central channel increases, which decreases the momentum flux ratio J, leading to less efficient mixing of air and fuel and, initially, a longer flame. However, as more air is mixed with the fuel in the central channel, Z_{st} drops as the amount of air from the coaxial flow needed to complete combustion decreases significantly, leading to a progressive shortening of the flame.

We can also observe the behavior of normalized flame length for a fixed value of Φ_1. For each series of Φ_1 in fixed color, Z_{st} is constant, and the trend is only affected by the momentum flux ratio J. For $J > 1$ in the leftmost part of Fig. 6, the annular flow momentum flux dominates, and a linear variation of the flame length is observed across all values of premixing equivalence ratio Φ_1. This is consistent with coaxial jet scaling laws developed by [28]. The slope decreases with Φ_1, with the non-premixed case $\Phi_1 = \infty$ showing the steepest slope. Following [28], this change in slope is attributed to the variation in the stoichiometric mixture fraction Z_{st}, also yielding a variable effect of burnt gases in the jet development. However, applying those corrections in the present

case does not produce a good overlapping for all the data, suggesting that another mechanism could also participate. This linear trend for L_f remains up to $J^{-1/2} \approx 2$.

In contrast, for $J \ll 1$ in the rightmost part of Fig. 6, the coaxial component becomes negligible, and a constant jet length is clearly retrieved for the lowest values of Φ_1. For Φ_1 = 4, the slope diminishes greatly, starting to resemble a plateau but still not flat, indicating that this might still be a transition zone. In the zone $J^{-1/2}$ >2, we observe this transition where the initial slopes progressively vary with $J^{-1/2}$ and Φ_{tot} getting larger.

From this, we can establish that varying staging heavily influences the flame's length. Based on previous literature, it is expected that NO_x emission also varies substantially. In addition, we see the most significant change in flame length occurs between Φ_1 = 4 and Φ_1 = 2, which also coincides with the appearance of the premixed flame front. As a result, the evolution of NO_x emissions is studied more finely between these two limits in the next section.

3 NO_X EMISSIONS: IMPACT OF STAGING AT $\mathcal{P}_{th}$= 10 KW.

3.1 Measurements

To investigate the role of staging on NO_x emissions in coaxial flames, a series of flame with constant parameters Φ_{tot}= 0.4, d_1 = 6 mm and $\mathcal{P}_{th}$= 10 kW is produced on the injector. The central equivalence ratio ranges from $\Phi_1 = \infty$ to Φ_1 = 2, with an increased number of flames between Φ_1 = 3.5 and Φ_1 = 2 to allow for a finer observation as the secondary flame front appears. In addition, two flames with d_1 = 10 mm at respectively Φ_1 = 6 and Φ_1 = 2 are produced to observe the effect of diameter under weak and strong staging conditions. In these experiments, the flames are confined in the combustion chamber described in Sec. 1.1. Both flame length and NO_x emissions are measured at every experimental point since emissions from hydrogen diffusion flames depend strongly on flame length and volume. As highlighted in Fig. 4, the flames in this work can display a secondary premixed flame front that could show a different behavior of NO_x production to the diffusion flame front. However, given the small NO_x production of premixed flames above an equivalence ratio of 2 in Fig. 1, we will neglect the rich premixed flame's contribution in our interpretation.

Figure 9 shows the evolution of the NO_x emission index as a function of the inverse of the internal equivalence ratio Φ_1. This quantity is proportional to the mass flow rate of air mixed with the fuel and represents the amount of air staging set in the injection. It shows that for d_1 = 6 mm, the staging effect is quite gradual. From $\Phi_1 = \infty$ to Φ_1 = 3.5, the $EINO_x$ decreases by about 0.1. From Φ_1 = 3.5 to Φ_1 = 2, the $EINO_x$ decreases by 0.5 while roughly the same amount of air has been added to the fuel. Low staging degrees are then not beneficial to reduce NO_x emissions. Two flames at d_1 = 10 mm are also plotted in this graph, for Φ_1 = 6 and Φ_1 = 2. No flame at $\Phi_1 = \infty$ is represented due to the blowout encountered at that point. These two flames show that, for this larger diameter, staging still decreases NO_x emissions. The decrease observed between the two flames at Φ_1 = 2 and 6 is lower than that observed for flames with smaller internal diameters. Nevertheless, the overall level of NO_x emissions remains below that of the flames at d_1 = 6 mm.

To understand more about the observed trends, Fig. 10 shows the plot of $EINO_x$ as a function of the measured flame length L_f from this series of flames. We observe that the NO_x emission index overall increases with flame length. The only outlier in this trend is the point with $\Phi_1 = \infty$ (non-premixed flame) that emits more NO_x than longer rich-premixed flames. At first, introducing a rich mixture instead of pure fuel appears to increase the flame length significantly, while at the same time, NO_x emissions remain quasi-constant. Increasing the proportion of air in the central channel further shortens the flame and reduces the $EINO_x$ by about 20% compared to the non-premixed case. The additional points with d_1 = 10 mm show a reduced flame length L_f. This is consistent with the observations on unconfined flames in Fig. 8 and explained by the lower $J^{-1/2}$ with a larger diameter d_1. These shorter flame lengths yield the lower NO_x emission levels observed for flames with d_1 = 10 mm in Fig. 9. Like the slighter decrease in $EINO_x$ for d_1 = 10 mm than for d_1 = 6 mm in Fig. 9, the reduction in flame length between Φ_1 = 6 and Φ_1 = 2 when d_1 = 10 mm is smaller. The flame length decreases by only around 1 cm with the larger diameter as opposed to 6 cm with the smaller diameter. The overall good correlation between $EINO_x$ and the flame lengths confirms the necessity to quickly mix the secondary air with the premixed flame's rich products to attenuate NO_x emission as in RQL systems.

One may also note that the decrease in flame length with increased staging is more significant

at lower values of Φ_1, as L_f declines by around 2 cm between Φ_1 = 2.25 and Φ_1 = 2 while between Φ_1 = 6 and Φ_1 = 3.5, this decrease is around 0.5 cm. This suggests that there could be a change in the mixing mechanism of the flame in this region. Figures 6 and 7 have highlighted the appearance and strengthening of the premixed flame front at the exit of the central channel. The nature of the diffusion flame front changes with air staging. In the non-premixed case, the flame front occurs between pure hydrogen and coaxial air. In the weakly staged case, the fuel side now includes oxygen due to the premixing, and the fresh gases' composition fed in the diffusion flame gradually changes as air staging is added. In the heavily staged case, the diffusion flame is supplied with a hot mixture of burned gases composed of hydrogen, water vapor, and nitrogen due to the premixed flame front. In this case, the new mixture condition can affect the mixing rules and could explain the observed further reduction in diffusion flame length for Φ_1 = 2.

In addition, the behavior of this type of flame under conditions of increased pressure and temperature like that of a gas turbine combustion chamber would be interesting to investigate. These conditions increase the laminar flame speed and might shift the operability range of the injector to higher equivalence ratios to avoid flashback. Furthermore, it can be expected that the amount of NO_x produced by the non-premixed flame front increases due to the higher availability of oxygen radicals [29]. In contrast, if the main NO_x pathway in the premixed flame is the nitrous oxide pathway, its NO_x emissions should be pressure independent.

3.2 Models

As mentioned in the introduction, extensive work was done to model the evolution of the NO_x emission index of non-premixed hydrogen flames with various parameters. As a result, we evaluate the performance of these models on our flames.

We can first observe the behavior of NO_x emission under the first scaling developed by Peters and Donnerhack [16] for jet flames. Figure 11 shows the evolution of $EINO_x$ with the residence time ${L^3}_f/({d_1}^2 u_1)$. Hence, the jet velocity also affects the NO_x emission in addition to the flame length effect discussed above. The $EINO_x$ profile is approaching proportionality with ${L^3}_f/({d_1}^2 u_1)$ across the various degrees of staging and the two diameters tested. The previous outlying point $\Phi_1 = \infty$ in Fig. 10 is now closer to the trend followed by the other conditions. As the abscissa takes

into account the change in bulk velocity and diameter, the points with d_1 = 10 mm follow closely the trend of the points with d_1 = 6 mm compared to the previous figures. While the agreement is satisfactory, the works in [17, 19] have outlined the need to account for a Damköhler effect (usually considered as a global aerodynamic strain rate), which could explain the dropping slope of the trend depicted in Fig. 11. Additionally, this scaling does not account for coflowing air or premixing.

Figure 12 reproduces the same scaling as the one in [20] where the global strain rate $(u_1 - u_2)/d_1$ in abscissa makes use of the presence of non-negligible coflow. The ordinate considers $EINO_x/(V_f/({d_1}^2 u_1))$ to remove the linear trend component due to the residence time. The volume of the flame V_f is calculated using the Otsu contour for the diffusion flame, with the assumption that the flames are axisymmetric. As the coflow velocity for the flame at d_1 = 10 mm and Φ_1 = 6 is higher than the fuel flow velocity, the absolute value $|u_1 - u_2|/d_1$ is retained. Two regimes can be distinguished in Fig. 12. First, at high strain, the scaled $EINO_x$ appears to increase with strain. This is due to the increase in super-equilibrium radicals as described in [17]. Moreover, the data fit relatively well with the half power law found in [17, 19, 20]. However, an opposite trend is observed at lower strain, with the emission decreasing with strain. A similar effect is observed in [21]. However, the change of trend also coincides with the change of diameter, which may mean that the internal diameter is responsible for these effects. More data is needed to discriminate between these two possibilities. However, it shows these simple models are insufficient to describe entirely the present flames and other effects must be taken into account.

4 ADDITIONAL PARAMETER VARIATIONS

Two additional parameters are studied: the flame thermal power and global equivalence ratio. Under constant Φ_{tot} and Φ_1, changing $\mathcal{P}_{th}$ scales all the flow rates by a common factor, thereby adjusting the velocities by a common factor. This, in turn, affects the residence time of the gases in the flame, which is expected to affect NO_x emissions. In addition, variations in the bulk velocity in the central channel also affect the stabilization of the premixed flame front. On the other hand, the global equivalence ratio Φ_{tot} is varied with $\mathcal{P}_{th}$ and Φ_1 constant, which corresponds to changing

the flow rate in the coflow.

4.1 Thermal Power

A study of thermal power is undertaken by examining two sets of three flames. In both sets, the global equivalence ratio Φ_{tot} is 0.4 while the central equivalence ratio Φ_1 is chosen to be equal to 2 to have a premixed flame front present to observe the effects of variations of bulk velocity in the central channel. The two sets have different internal diameters d_1: d_1 = 6 mm and d_1 = 10 mm. Each set corresponds to a fixed momentum flux ratio. $J = 0.09$ for the first set and 1.25 for the second.

The Abel-inverted OH* chemiluminescence images from the first set are shown in Fig. 13. With increasing thermal power, the length of the premixed flame becomes higher in absolute value and when compared to the diffusion flame's height. Between the lowest and highest thermal power flame, there is a threefold increase in bulk velocity while a twofold rise in premixed flame length is measured. As momentum flux ratio J and equivalence ratios are fixed while varying the power, the diffusion flame length sees comparably smaller variations that may be linked to the changes in premixed flame length. Corresponding NO_x emissions are reported in Table 2. $EINO_x$ decreases as thermal power increases with a stark decrease in NO_x between 5 kW and 10 kW. Since the flame length only marginally changes, the residence time follows a threefold reduction with the increasing bulk velocity and explains mainly the drop in NO_x at larger power. When analyzing the emissions scaled by the residence time in the flame (third row in Tab. 2), they increase with the velocity difference $|u_1 - u_2|$ (sixth row), which is coherent with the observations in Fig. 12. Indeed, with higher thermal power, the strain increases, causing an increase in super-equilibrium radicals. This contribution slows down the $EINO_x$ decrease at 15 kW.

The results for the second set of flames with d_1 = 10 mm are shown in Table 3. In this set of flame shown in Fig. 14, the difference in velocity between the internal channel and the coflow is smaller (around 7 m·s^{-1} for the highest power case against 90 m·s^{-1}) due to the increased internal diameter. The flames display a much shorter premixed flame front (see Fig. 14) across all values of thermal power due to the reduced bulk velocity with the larger diameter. One might note that the lowest thermal power used with this diameter is 6.5 kW instead of 5 kW. This is because the low

velocities at 5 kW caused a flashback of the flame. Other than this, flashback was not encountered when operating the burner. The same trend as the first set is observed with EINO$_x$ decreasing with thermal power. However, it can be noticed that the flame gets here slightly longer with larger thermal power. The trend in scaled EINO$_x$ is similar to the first set for $d_1 = 6$ mm, as it increases with $\mathcal{P}_{th}$. The observations of Fig. 12 were in opposition where strain appeared to reduce the scaled EINO$_x$ at lower strain rates. This suggests that there might be another mechanism involved when the change in lower strain rates is induced by Φ_1.

4.2 Global Equivalence Ratio

The other study concerning the global equivalence ratio is undertaken by studying flames at Φ_{tot} = 0.35 and Φ_{tot} = 0.45 with a constant flame thermal power $\mathcal{P}_{th}$ = 10 kW for $\Phi_1 = \infty$, 6 and 2 when d_1 = 6 mm, and Φ_1 = 6 and 2 when d_1 = 10 mm (due to blow-off occurring when $\Phi_1 = \infty$). To verify if the behavior observed in Fig. 11 is affected by coaxial air flow, these additional flames are plotted on the same EINO$_x$ - ${L^3}_f/({d_1}^2 u_1)$ graph in Fig. 15. Furthermore, as d_1 and u_1 stay constant under variations of Φ_{tot}, it allows us to observe the qualitative evolution of L_f with coaxial air. In all cases, increasing the global equivalence ratio increases flame length, consistently with the discussion of Fig. 8. This effect is the strongest for the non-premixed flames. Likewise, increasing the global equivalence ratio in all flames also increases the measured EINO$_x$. This follows the increase in residence time induced by the added flame length for fixed u_1 but the trend of the added points step aside from the previous data series for Φ_{tot} = 0.4. Clearly, the residence time alone cannot overlap the data. Updating Fig. 12, which already experienced some limitations at low strain rates, was inconclusive.

To better fit the trends observed for these flames, we turn to the work of Weiland et al. [21], who, with some intuition, devised a model that accurately represented nitrogen-diluted hydrogen flames with coaxial air. Using the far-field scaling law of Dahm and Mayman [18] for jet length as a function of fuel channel diameter, a scaling law of $EINO_x/(V_f/(u_1{d_1}^2))$ as a function of $\frac{u_1}{d_1}\frac{d_1^*}{L_f} \approx \frac{u_1}{d_1} Z_{st} \left(1 + \frac{\dot{m}_2 u_2}{\dot{m}_1 u_1}\right)^{1/2}$ was devised. Where $d_1^* = d_1\sqrt{\frac{\rho_1}{\rho 2}}$, Z_{st} is the stoichiometric mixture fraction of the fuel mixture and $\dot{m}_i u_i$ is the integrated momentum flux of a given channel. In our flames, Z_{st} ranges from 0.028 in the non-premixed case to 0.51 when Φ_1=2. For nitrogen-diluted

hydrogen flames with coaxial air, this scaling was found to give a 1/2 power law, as observed previously in simple jet flame [17]. This suggests that it captures the effect of Damköhler number in that work. This scaling law is applied to all the studied flame conditions. Results are shown in Fig. 16. All the points do not lie on a single curve. Two groups of points, however, present a linear pattern of about the same slope in the logarithmic plot. The first group of points contains the non-premixed flames and the flames with d_1 = 10 mm, while the other one includes the premixed flame with d_1 = 6 mm. The main difference between these two groups is the momentum flux ratio: J$>$1 in the first group, while the other corresponds to flames with J$<$1. This separation between the two sets of points suggests that the far-field scaling law from [18] may not be as good in both regimes. The data collapse is improved in Fig. 17 in which $\frac{d_1^*}{L_f}$ is directly used instead. In this figure, all the points follow the same trend along a 1/2 power law. The result makes us believe that $\frac{u_1}{L_f}$ can better represent the mixing time scale to account for the Damköhler-number effects. The reason why remains, however, still elusive as in [21] and will require further analysis.

5 CONCLUSION

Staged flames with rich premixing and coflowing air have been stabilized on a coaxial injector. The effect of air staging between the two channels on flame length, topology, and NO_x emission has been studied. It was first seen that introducing a rich mixture of fuel and air could reduce the total flame length compared to a non-premixed injection thanks to the modified stoichiometric mixture fraction between both streams. In addition, when nearing a central equivalence ratio of Φ_1=2, a premixed flame front is stabilized and further reduces flame length. Air staging in the coaxial injector also reduces the NO_x emission index, primarily through its reduction of the diffusion flame height that is responsible for NO_x production. The variations in flame thermal power have shown that the flame global strain rate also significantly affect the NO_x emission. Models used in non-premixed flames have been tested and have shown to be ill-adapted to the studied flames. The model by [21] was applied and appeared to yield promising results for studied flames. Future work will include additional diagnostics on the instantaneous velocity field and the presence and position of flame fronts. This detailed knowledge will nourish modeling efforts of flame lengths and

emissions.

Further reduction in NO_x emissions should also be sought. Increasing the internal diameter, in particular, would allow bulk velocities and momentum flux ratios that could not be reached with the existing design. Mixing enhancement with swirl to promote shorter flames is also envisioned.

In addition, study of the injector under high-pressure, as well as burning blends of hydrogen and natural gas would allow to evaluate practical applications of the injection method.

ACKNOWLEDGEMENTS

This work was funded by CIFRE contract 2021/1697 from Agence Nationale de la Recherche et de la Technologie and Safran Tech.

REFERENCES

[1] Brewster, B. S., Cannon, S. M., Farmer, J. R. and Meng, F. "Modeling of lean premixed combustion in stationary gas turbines." *Progress in Energy and Combustion Science* Vol. 25 No. 4 (1999): pp. 353–385. 10.1016/S0360-1285(98)00014-8.

[2] Ren, X., Xue, X., Brady, K. B., Sung, C.-J. and Mongia, H. C. "Fundamental investigations for lowering emissions and improving operability." *Propulsion and Power Research* Vol. 7 No. 3 (2018): pp. 197–204. 10.1016/j.jppr.2018.07.001.

[3] Feitelberg, A. S. and Lacey, M. A. "The GE Rich-Quench-Lean Gas Turbine Combustor." *Journal of Engineering for Gas Turbines and Power* Vol. 120 No. 3 (1998): pp. 502–508. 10.1115/1.2818173.

[4] Marek, C., Smith, T. and Kundu, K. "Low Emission Hydrogen Combustors for Gas Turbines Using Lean Direct Injection." *41st AIAA/ASME/SAE/ASEE Joint Propulsion Conference & Exhibit*. Joint Propulsion Conferences. American Institute of Aeronautics and Astronautics (2005). 10.2514/6.2005-3776.

[5] Reichel, T. G., Goeckeler, K. and Paschereit, O. "Investigation of Lean Premixed Swirl-Stabilized Hydrogen Burner With Axial Air Injection Using OH-PLIF Imaging." *Journal of Engineering for Gas Turbines and Power* Vol. 137 No. 11 (2015): p. 111513. 10.1115/1.4031181.

[6] Lee, T. and Kim, K. T. "Combustion dynamics of lean fully-premixed hydrogen-air flames in a mesoscale multinozzle array." *Combustion and Flame* Vol. 218 (2020): pp. 234–246. 10.1016/j.combustflame.2020.04.024.

[7] Funke, H. H.-W., Beckmann, N., Keinz, J. and Horikawa, A. "30 Years of Dry-Low-NOx Micromix Combustor Research for Hydrogen-Rich Fuels—An Overview of Past and Present Activities." *Journal of Engineering for Gas Turbines and Power* Vol. 143 No. 7 (2021): p. 071002. 10.1115/1.4049764.

[8] Agarwal, P., Sun, X., Gauthier, P. Q. and Sethi, V. "Injector Design Space Exploration for an Ultra-Low NOx Hydrogen Micromix Combustion System." *Proceedings of the ASME Turbo Expo 2019: Turbomachinery Technical Conference and Exposition*. V003T03A013. Phoenix, AZ, June 17-21, 2019. 10.1115/GT2019-90833.

[9] Ranzi, E., Frassoldati, A., Grana, R., Cuoci, A., Faravelli, T., Kelley, A. P. and Law, C. K. "Hierarchical and comparative kinetic modeling of laminar flame speeds of hydrocarbon and oxygenated fuels." *Progress in Energy and Combustion Science* Vol. 38 No. 4 (2012): pp. 468–501. 10.1016/j.pecs.2012.03.004.

[10] Song, Y., Marrodán, L., Vin, N., Herbinet, O., Assaf, E., Fittschen, C., Stagni, A., Faravelli, T., Alzueta, M. U. and Battin-Leclerc, F. "The sensitizing effects of NO2 and NO on methane low temperature oxidation in a jet stirred reactor." *Proceedings of the Combustion Institute* Vol. 37 No. 1 (2019): pp. 667–675. 10.1016/j.proci.2018.06.115.

[11] Shudo, T., Omori, K. and Hiyama, O. "NOx reduction and NO2 emission characteristics in rich-lean combustion of hydrogen." *International Journal of Hydrogen Energy* Vol. 33 No. 17 (2008): pp. 4689–4693. 10.1016/j.ijhydene.2008.05.034.

[12] Göke, S., Füri, M., Bourque, G., Bobusch, B., Göckeler, K., Krüger, O., Schimek, S., Terhaar, S. and Paschereit, C. O. "Influence of steam dilution on the combustion of natural gas and hydrogen in premixed and rich-quench-lean combustors." *Fuel Processing Technology* Vol. 107 (2013): pp. 14–22. 10.1016/j.fuproc.2012.06.019.

[13] Marragou, S., Magnes, H., Poinsot, T., Selle, L. and Schuller, T. "Stabilization regimes and pollutant emissions from a dual fuel CH4/H2 and dual swirl low NOx burner." *International*

Journal of Hydrogen Energy Vol. 47 No. 44 (2022): pp. 19275–19288. 10.1016/j.ijhydene.2022.04.033.

[14] Leroy, M., Mirat, C., Renaud, A. and Vicquelin, R. "Stabilization of Low-NOx Hydrogen Flames on a Dual-Swirl Coaxial Injector." *Journal of Engineering for Gas Turbines and Power* Vol. 145 No. 2 (2022): p. 021021. 10.1115/1.4055711.

[15] Minakawa, K. and Yuasa, S. "Study on Hydrogen Combustors with Two-Staged Combustion Method for Micro Gas Turbines." *Journal of Environment and Engineering* Vol. 2 No. 3 (2007): pp. 590–600. 10.1299/jee.2.590.

[16] Peters, N. and Donnerhack, S. "Structure and similarity of nitric oxide production in turbulent diffusion flames." *Symposium (International) on Combustion* Vol. 18 No. 1 (1981): pp. 33–42. 10.1016/S0082-0784(81)80008-2.

[17] Chen, R.-H. and Driscoll, J. F. "Nitric oxide levels of jet diffusion flames: Effects of coaxial air and other mixing parameters." *Symposium (International) on Combustion* Vol. 23 No. 1 (1991): pp. 281–288. 10.1016/S0082-0784(06)80271-7.

[18] Dahm, W. J. A. and Mayman, A. G. "Blowout limits of turbulent jet diffusion flames for arbitrary source conditions." *AIAA Journal* Vol. 28 No. 7 (1990): pp. 1157–1162. 10.2514/3.25186.

[19] Driscoll, J. F., Chen, R.-H. and Yoon, Y. "Nitric oxide levels of turbulent jet diffusion flames: Effects of residence time and Damkohler number." *Combustion and Flame* Vol. 88 No. 1 (1992): pp. 37–49. 10.1016/0010-2180(92)90005-A.

[20] Chen, J. Y. and Kollmann, W. "PDF modeling and analysis of thermal NO formation in turbulent nonpremixed hydrogen-air jet flames." *Combustion and Flame* Vol. 88 No. 3 (1992): pp. 397–412. 10.1016/0010-2180(92)90042-N.

[21] Weiland, N., Chen, R. H. and Strakey, P. "Effects of coaxial air on nitrogen-diluted hydrogen jet diffusion flame length and NOx emission." *Proceedings of the Combustion Institute* Vol. 33 No. 2 (2011): pp. 2983–2989. 10.1016/j.proci.2010.06.075.

[22] Jourdaine, P., Mirat, C., Caudal, J. and Schuller, T. "Stabilization Mechanisms of Swirling Premixed Flames With an Axial-Plus-Tangential Swirler." *Journal of Engineering for Gas Turbines and Power* Vol. 140 No. 8 (2018): p. 081502. 10.1115/1.4038617.

[23] Degenève, A., Jourdaine, P., Mirat, C., Caudal, J., Vicquelin, R. and Schuller, T. "Effects of a Diverging Cup on Swirl Number, Flow Pattern, and Topology of Premixed Flames." *Journal of Engineering for Gas Turbines and Power* Vol. 141 No. 3 (2018): p. 031022. 10.1115/1.4041518.

[24] Schefer, R. W., Kulatilaka, W. D., Patterson, B. D. and Settersten, T. B. "Visible emission of hydrogen flames." *Combustion and Flame* Vol. 156 No. 6 (2009): pp. 1234–1241. 10.1016/j.combustflame.2009.01.011.

[25] Degenève, A., Vicquelin, R., Mirat, C., Labegorre, B., Jourdaine, P., Caudal, J. and Schuller, T. "Scaling relations for the length of coaxial oxy-flames with and without swirl." *Proceedings of the Combustion Institute* Vol. 37 No. 4 (2019): pp. 4563–4570. 10.1016/j.proci.2018.06.032.

[26] Otsu, N. "A Threshold Selection Method from Gray-Level Histograms." *IEEE Transactions on Systems, Man, and Cybernetics* Vol. 9 No. 1 (1979): pp. 62–66. 10.1109/TSMC.1979.4310076.

[27] Becker, H. A. and Yamazaki, S. "Entrainment, momentum flux and temperature in vertical free turbulent diffusion flames." *Combustion and Flame* Vol. 33 (1978): pp. 123–149. 10.1016/0010-2180(78)90055-X.

[28] Schumaker, S. A. and Driscoll, J. F. "Coaxial turbulent jet flames: Scaling relations for measured stoichiometric mixing lengths." *Proceedings of the Combustion Institute* Vol. 32 No. 2 (2009): pp. 1655–1662. 10.1016/j.proci.2008.06.051.

[29] Correa, S. M. "A Review of NOx Formation Under Gas-Turbine Combustion Conditions." *Combustion Science and Technology* Vol. 87 No. 1-6 (1993): pp. 329–362. 10.1080/00102209208947221.

Table 1. PARAMETER VALUES FOR FLAMES IN FIG. 10

Parameter	Range	Parameter	Range
J [-]	0.09-7.2	Φ_{tot} [-]	0.4
Re_1 [-]	2000 - 18000	u_1 [m·s^{-1}]	18.2-73.9
Re_2 [-]	12500-17000	u_2 [m·s^{-1}]	18.3-28.2
$\mathcal{P}_{th}$ [kW]	10	Pressure [atm]	1

Table 2. NOx EMISSIONS AT VARIOUS THERMAL POWERS FOR Φ_1=2, Φ_{tot}=0.4, d_1= 6 mm.

$\mathcal{P}_{th}$ [kW]	5	10	15
$EINO_x$ [g/kgH_2]	4.47	2.52	1.99
$EINO_x/(V_f/({u_1}{d_1}^2))$ [g/(kgH_2·s)]	161	178	236
L_f [cm]	20.4	18.4	18.8
L_p [cm]	3.4	5.4	7.7
$\lvert u_1 - u_2 \rvert$ [m·s^{-1}]	30.0	60.3	90.0

Table 3. NOx EMISSIONS AT VARIOUS THERMAL POWERS FOR Φ_1=2, Φ_{tot}=0.4, d_1= 10 mm.

$\mathcal{P}_{th}$ [kW]	6.5	10	15
$EINO_x$ [g/kgH_2]	2.78	2.32	1.96
$EINO_x/(V_f/({u_1}{d_1}^2))$ [g/(kgH_2·s)]	122	135	167
L_f [cm]	13.3	14.4	14.9
L_p [cm]	1.9	2.5	3.1
$\lvert u_1 - u_2 \rvert$ [m·s^{-1}]	2.6	4.3	6.6

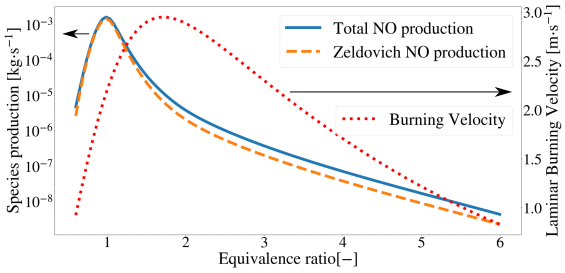

Fig. 1. NO_x production (premixed flames with a 15-cm long domain) and laminar burning velocity of hydrogen-air flames as a function of equivalence ratio under standard pressure and temperature.

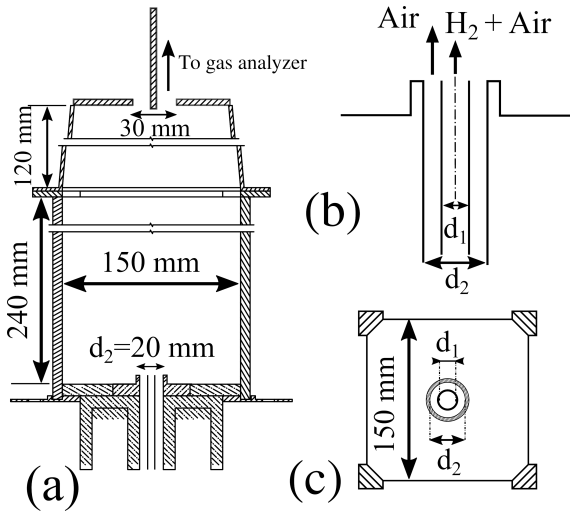

Fig. 2. (a) Sketch of the square-section combustion chamber. (b) Sketch of the coaxial injector. (c) Sketch of the injector exit plane.

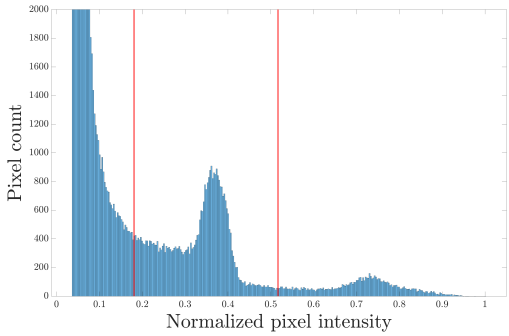

Fig. 3. Histograms of an OH* image. Φ_{tot} = 0.4, Φ_1 = 2, $\mathcal{P}_{th}$= 15 kW.

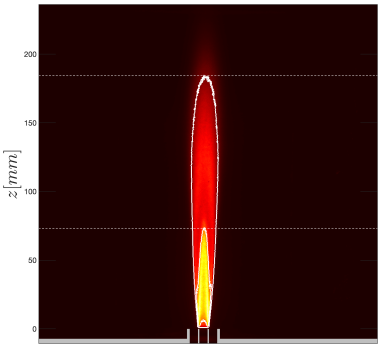

Fig. 4. Flame OH* image (line-of-sight integrated) for Φ_{tot} = 0.4, Φ_1 = 2, $\mathcal{P}_{th}$= 15 kW, associated Otsu contours (plain white lines) and corresponding flame lengths (horizontal dashed lines).

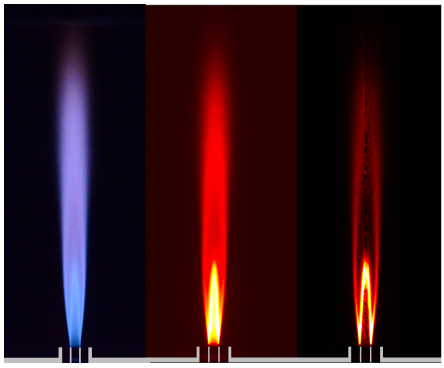

Fig. 5. Dual flame fronts visualization. From left to right: Visible range, OH* chemiluminescence, Abel-inverted OH* chemiluminescence. Φ_{tot} = 0.35, Φ_1 = 2, $\mathcal{P}_{th}$= 10 kW.

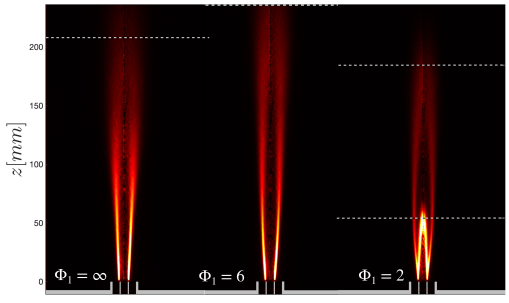

Fig. 6. Abel-inverted OH* chemiluminescence images under varying degrees of air staging. Φ_{tot}=0.4, $\mathcal{P}_{th}$=10 kW.

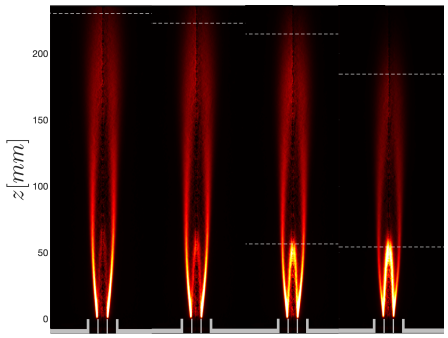

Fig. 7. Abel-inverted OH* chemiluminescence images at various values of Φ_1 with d_1 = 6 mm, Φ_{tot}=0.4 and $\mathcal{P}_{th}$=10 kW. From left to right: Φ_1=3.5, 3, 2.5, 2.

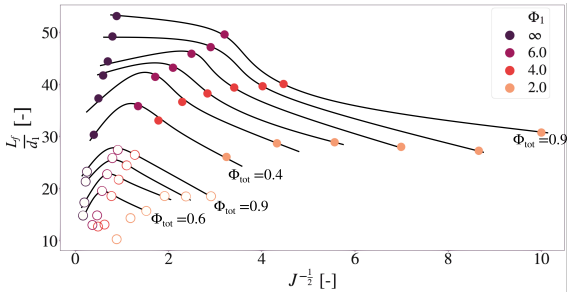

Fig. 8. Flame length L_f as a function of $J^{-\frac{1}{2}}$ for different air staging conditions indicated by Φ_1: closed symbols ●: d_1 = 6 mm; open symbols ○: d_1 = 10 mm.

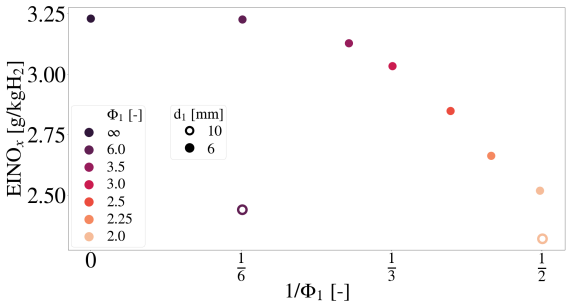

Fig. 9. EINO$_x$ for various air staging conditions with d_1 = 6 mm, Φ_{tot}=0.4 and $\mathcal{P}_{th}$= 10 kW.

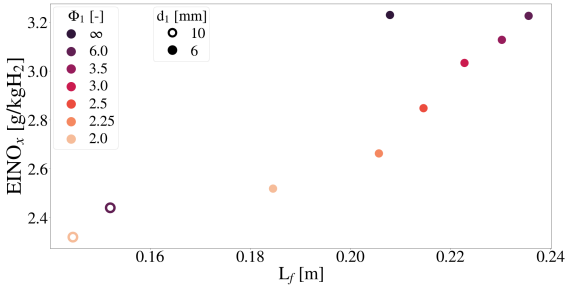

Fig. 10. EINO$_x$ as a function of flame length for the same operating conditions as in Fig. 9.

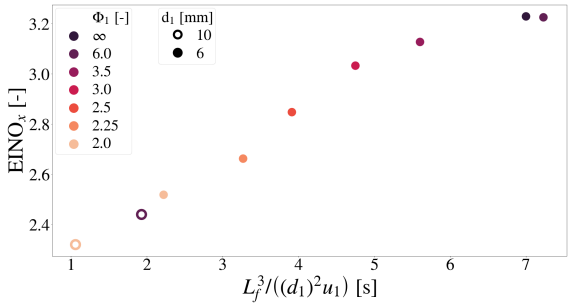

Fig. 11. EINO$_x$ as a function of residence time ${L^3}_f/({d_1}^2 u_1)$. Φ_{tot}=0.4 , $\mathcal{P}_{th}$ = 10 kW.

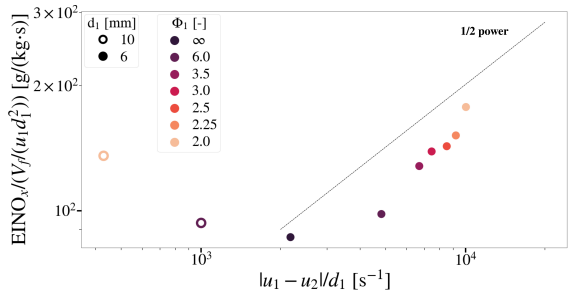

Fig. 12. Scaled EINO$_X$ following [20] as a function of the coaxial global strain rate in a logarithmic plot. Φ_{tot}=0.4 and $\mathcal{P}_{th}$= 10 kW.

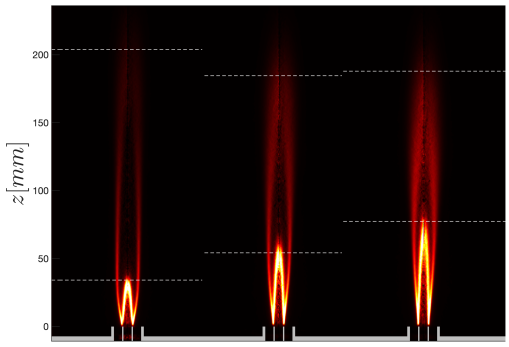

Fig. 13. Abel-inverted OH* chemiluminescence images at various thermal powers for d_1 = 6 mm, Φ_1=2, Φ_{tot}=0.4. From left to right: $\mathcal{P}_{th}$=5, 10, 15 kW.

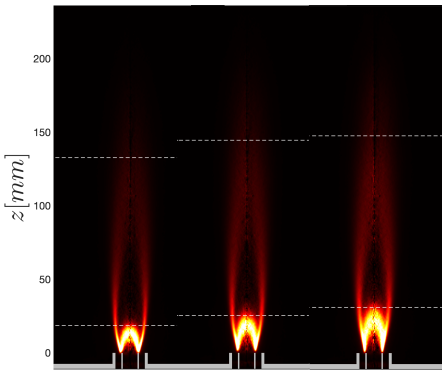

Fig. 14. Abel-inverted OH* chemiluminescence images at various thermal powers for d_1 = 10 mm. Φ_1=2, Φ_{tot}=0.4, $\mathcal{P}_{th}$=6.5, 10, 15 kW.

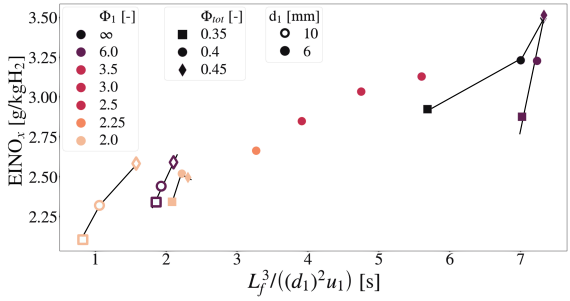

Fig. 15. EINO$_x$ as a function of flame residence time $L^3{}_f/(d_1{}^2u_1)$ for different values of Φ_{tot}.

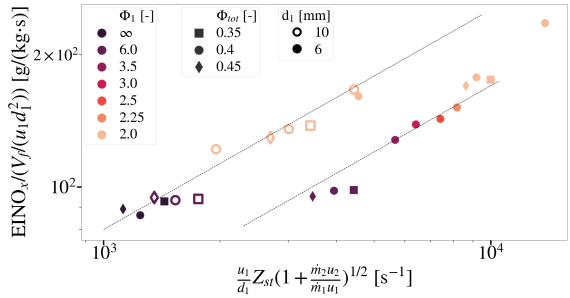

Fig. 16. Scaled EINO$_x$ as a function of a modified strain rate u_1/d_1 (see corrective factor in axis title) plotted in a logarithmic plot.

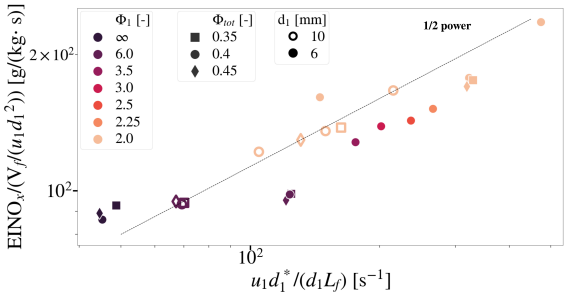

Fig. 17. Scaled EINO$_x$ as a function of modified strain rate $\frac{u_1}{d_1}\frac{{d_1}^*}{L_f}$ plotted in a logarithmic plot.